PHILOSOPHICAL TRANSACTIONS OF THE ROYAL SOCIETY A MATHEMATICAL, PHYSICAL & ENGINEERING SCIENCES

The Dissolution of Calcite at pH > 7: Kinetics and Mechanism

R. G. Compton and K. L. Pritchard

Phil. Trans. R. Soc. Lond. A 1990 **330**, 47-70
doi: 10.1098/rsta.1990.0002

Phil. Trans. R. Soc. Lond. A **330**, 47–70 (1990) [47]
Printed in Great Britain

THE DISSOLUTION OF CALCITE AT pH > 7: KINETICS AND MECHANISM

BY R. G. COMPTON AND K. L. PRITCHARD
Physical Chemistry Laboratory, University of Oxford, South Parks Road, Oxford OX1 3QZ, U.K.

(*Communicated by J. S. Rowlinson, F.R.S.* – *Received* 5 *August* 1988 – *Revised* 7 *February* 1989)

CONTENTS

A technique is described that allows an assessment of the various candidate rate laws that have been proposed to predict the dissolution kinetics of calcite under high pH conditions. A combination of theoretical modelling and experimentation allows us to choose the following rate law as that which best fits the observed data:

$$\text{rate (mol cm}^{-2}\text{ s}^{-1}) = k - k'[\text{Ca}^{2+}]_s\,[\text{CO}_3^{2-}]_s,$$

where $k' = k/K_{sp}$ and K_{sp} is the solubility product of calcium carbonate. The modelling developed differs from previous studies in that it deals in terms of surface concentrations of reactants, $[\text{Ca}^{2+}]_s$ and $[\text{CO}_3^{2-}]$, as opposed to those present in bulk solution.

1. INTRODUCTION

In the previous paper (Compton & Unwin 1989) the importance of the investigation of the dissolution of calcium carbonate in aqueous solution, and its relevance to problems of an industrial and environmental nature, was discussed. The problems and limitations of traditional techniques hitherto used, such as absence of well-defined hydrodynamics and the lack of control over surface morphology of the sample, were defined. A general experimental methodology whereby these difficulties could be overcome was presented. The basic idea of this technique is to flow a solution over the surface of the crystal and then to detect either unreacted reactants or reaction products downstream of the crystal, by potentiometric or by amperometric

methods. This method was used to study calcite dissolution under acidic, i.e. pH < 4, conditions and in this paper we use a similar methodology to investigate the dissolution at higher pH (greater than 7) and in the absence of CO_2.

Many equations have been proposed that attempt to model the dissolution of calcium carbonate under the conditions of interest. Some of these equations are empirical in nature, others have a more mechanistic basis. One of the former type is that of Dorange & Guetchidjan (1978) who studied the dissolution of marble chips over a range of partial pressures of CO_2 and background Ca^{2+} concentrations. They proposed that the rate of dissolution was determined simply by the distance of the system from equilibrium, i.e.

$$\text{rate} = K^*_{DG}([Ca^{2+}]_{eq} - [Ca^{2+}]). \tag{1}$$

Sjöberg (1976) did experiments on powdered calcite samples and established the following equation for the dissolution rate

$$\text{rate} = K_s(K_{sp}^{\frac{1}{2}} - [Ca^{2+}]^{\frac{1}{2}}[CO_3^{2-}]^{\frac{1}{2}}), \tag{2}$$

where K_{sp} is the calcite solubility product, $[Ca^{2+}]$ and $[CO_3^{2-}]$ are the bulk calcium and carbonate concentrations, and K_s is a rate constant.

A rate equation based on a mechanistic model of dissolution was proposed by Plummer *et al.* (1978) in which the rate is given by,

$$\text{rate} = k_1 a_{H^+} + k_2 a_{HCO_3^-} + k_3 a_{H_2O} - k_4 a_{Ca^{2+}} a_{HCO_3^-}, \tag{3}$$

where a_x denotes the bulk solution activity of species x and k_1, k_2, k_3 and k_4 are rate constants. In the absence of CO_2, and because for pH > 7 the first term is negligible, equation (3) reduces to

$$\text{rate} = k_3' - k_4 a_{Ca^{2+}} a_{HCO_3^-}. \tag{4}$$

This equation implies that there is a forward reaction with water, which continues at a constant rate, and a back reaction that is dependent upon the activity of calcium and bicarbonate ions. Whereas Plummer *et al.* assumed that it was appropriate to work with bulk activities, or concentrations, in this work we will use surface quantities for the reasons alluded to subsequently. Thus in the modelling described below we will adopt a form of equation (4) in which $a_{Ca^{2+}}$ and $a_{HCO_3^-}$ are replaced by $[Ca^{2+}]_s$ and $[HCO_3^-]_s$, where the subscript denotes the surface value and we have chosen to work with concentrations rather than activities, which is a reasonable approximation under conditions of fixed ionic strength.

In principle other mechanistic rate laws of the general form of (4) are conceivable, i.e.

$$\text{rate} = k - k_1[Ca^{2+}]_s[CO_3^{2-}]_s \tag{5}$$

or

$$\text{rate} = k - k_1[Ca^{2+}]_s[CO_3^{2-}]_s - k_2[Ca^{2+}]_s[HCO_3^-]_s. \tag{6}$$

If we assume that equilibrium is reached when the product of the surface concentrations of Ca^{2+} and CO_3^{2-} equals the solubility product, we may show that equations (4), (5) and (6) reduce to the same form. To this end consider equation (4), which we may write as

$$\text{rate} = k - k_1[Ca^{2+}]_s[HCO_3^-]_s.$$

We know that

$$[HCO_3^-] = [CO_3^{2-}][H^+]/K_A,$$

where K_A is the second dissociation constant of carbonic acid, and so we can write

$$\text{rate} = k - (k_1[Ca^{2+}]_s\,[CO_3^{2-}]_s\,[H^+]_s/K_A). \tag{7}$$

Now when the product $[Ca^{2+}]_s\,[CO_3^{2-}]_s$ equals the solubility product of calcite the rate must equal zero, so

$$k_1 = kK_A/[H^+]_s\,K_{sp}.$$

If we substitute this expression into equation (7) we get,

$$\text{rate} = k - (kK_A[Ca^{2+}]_s\,[HCO_3^-]_s/[H^+]_s\,K_{sp}). \tag{8}$$

But
$$K_A[HCO_3^-]_s/[H^+]_s = [CO_3^{2-}]_s,$$

thus from equation (8) we find that

$$\text{rate} = k - (k/K_{sp})\,[Ca^{2+}]_s\,[CO_3^{2-}]_s. \tag{9}$$

Consider next equation (5). We can again put the rate equal to zero when the product $[Ca^{2+}]_s\,[CO_3^{2-}]_s$ equals the calcite solubility product, from which it follows that

$$k_1 = k/K_{sp},$$

and so
$$\text{rate} = k - (k/K_{sp})\,[Ca^{2+}]_s\,[CO_3^{2-}]_s,$$

which is of the same form as (9).

We next consider equation (6). At equilibrium

$$k = [Ca^{2+}]_s\,(k_1[CO_3^{2-}]_s + k_2[HCO_3^-]_s), \tag{10}$$

and substituting
$$[HCO_3^-]_s = [CO_3^{2-}]_s\,[H^+]_s/K_A$$

into equation (10) we obtain

$$k = [Ca^{2+}]_s\,(k_1[CO_3^{2-}]_s + (k_2[CO_3^{2-}]_s\,[H^+]_s/K_A)),$$

or
$$k = K_{sp}(k_1 + (k_2[H^+]_s/K_A)).$$

We may then substitute for k_1 in equation (6):

$$\begin{aligned}\text{rate} &= k - \left(\frac{k}{K_{sp}} - \frac{k_2[H^+]}{K_A}\right)[Ca^{2+}]_s\,[CO_3^{2-}]_s - \frac{k_2[Ca^{2+}]_s\,[CO_3^{2-}]_s\,[H^+]_s}{K_A}\\ &= k - (k/K_{sp})\,[Ca^{2+}]_s\,[CO_3^{2-}]_s,\end{aligned}$$

which again has the same form as equation (9). Thus we have shown how, under the assumption that dissolution ceases when the calcite solubility product is reached, the rate laws (4), (5) and (6) may be reduced to the same kinetic form. One may conclude that kinetic analysis at a fixed pH alone cannot distinguish between the three mechanisms implied by these three equations.

In this paper we develop a numerical computational method whereby we can model the dissolution for any of the given rate equations. The crucial difference between this work and all previous modelling is that we consider surface concentrations in our rate equations. As pointed out elsewhere (Sjöberg & Rickard 1984), the very nature of the dissolution process dictates that it is the concentrations of species at the surface that control the reaction or indeed

any heterogeneous process. Thus using these instead of bulk solution concentrations should give us much more detailed information concerning the kinetics and mechanisms involved. By a comparison of experimental data with that predicted by our modelling work we may deduce which of the above candidate equations best reflects the true processes controlling dissolution. Of course the surface concentrations may be related to bulk concentrations, but only if the prevailing mass transport conditions are known. Although this is indeed the case in the experiments described here because of the defined hydrodynamics of the flow cell, this will not generally be so. In particular, for the case of dissolving powders it will be extremely difficult to relate the two. Thus the use of surface concentrations is the only general way of writing rate equations for the calcite dissolution reaction.

2. Experimental

Experiments were done using the flow cell previously described and characterized (Compton & Unwin 1990). In essence, this consists of a rectangular duct cut in a perspex block and closed by a cover plate. The latter comprises a crystal of calcite (Roger Taylor Minerals, Surrey, U.K.) cast into a resin block (Araldite, Ciba-Geigy). This cover plate may be polished smooth by the use of diamond lapping compounds (Engis Ltd) of progressively finer grit size, so that the crystal is flat and lies flush with the surface. Incorporated into the cover plate is a flat membrane pH electrode (MI-404, Microelectrodes Inc.), which is located immediately downstream of the crystal. The flux of calcium ions leaving the crystal surface is detected with a calcium ion selective electrode (ISE) (MI-600, Microelectrodes Inc.) located in a mixing chamber as shown in figure 1. Dye injection experiments (using fluorescein in aqueous alkali) showed that material arriving in the mixing chamber was fully homogenized before detection at the calcium sensor. Thus the latter responded to the average bulk calcium concentration of the solution leaving the zone of the dissolving crystal. Typical experiments involved a channel 3 cm long, 0.138 cm deep and 0.57 cm wide, a crystal of length 0.66 cm and flow rates of between 1×10^{-3} and 0.5 $cm^3\ s^{-1}$.

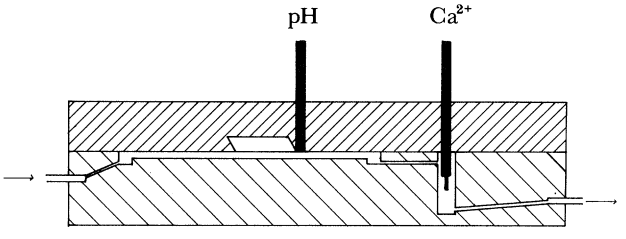

Figure 1. A schematic diagram of the channel unit showing the position of the potentiometric electrodes.

Solutions were made up using triply distilled de-ionized water (resistivity > 18 $M\Omega\ cm^{-2}$) and AnalaR grade reagents. All solutions were made up to a total ionic strength of 0.5 mol dm^{-3} using KCl and were degassed for several hours with argon to expel CO_2. The solution was adjusted, by the addition of NaOH or HCl, to the required pH. Solutions were placed in a reservoir and fed by gravity through the channel and so over the crystal. The flow was controlled by the height of feed and a pre-calibrated capillary placed downstream of the channel. The block containing the channel was placed in a thermostatted box held at

(25±0.2) °C. The box and all solution feed tubes were argon jacketed to exclude CO_2 thoroughly.

The range of Ca^{2+} concentrations encountered during these experiments varied between 1×10^{-7} and 1×10^{-6} mol dm^{-3}. Unfortunately this lay outside the region of linear response of the electrode used. Thus the possible experimental error was too large to allow the Ca^{2+} electrode to be used to discriminate between the possible mechanisms. However, the readings obtained did show that Ca^{2+} concentrations to be of the same order of magnitude as those predicted by the modelling work.

3. Theory

In this section, theory is derived that relates the potentiometric response at both the pH and calcium ion-selective electrodes in the flow system to the mechanism of the dissolution taking place at the calcite surface and identifies the influence of solution flow rate and flow cell geometry. As indicated above, it is the dissolution process under conditions of pH > 7 that is of interest in this paper. However, because the relevant convective-diffusion equations for the process under consideration have to be solved by a numerical procedure (the 'backwards implicit finite difference (BIFD) method') we first tackle the corresponding problem for the dissolution of calcite at around pH 3.0 under conditions where the process is known to be controlled by the rate of transport of H^+ to the crystal surface. The reason for this is that under these conditions the sought responses can be deduced analytically. The corresponding low pH problem is then tackled numerically via the BIFD method and comparison of the results of the two approaches used to validate the computational method. Finally the high pH problem is addressed using the BIFD approach. The various dissolution mechanisms detailed in the introduction are considered in turn and, for each, the signal on the pH electrode and the Ca^{2+} ISE are related to the flow cell geometry, solution flow rate and the kinetic parameters in the selected calcite dissolution rate equation.

(*a*) *Low* pH *region*

(i) *Analytical solution*

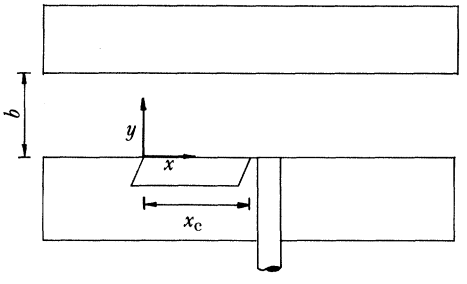

Figure 2. The coordinate system used in both the numerical and analytical solutions.

In this section, the response of the pH electrode downstream of the dissolving calcite crystal is calculated for the case where the calcite dissolution is assumed to take place via rate determining mass transport of H^+ to the crystal surface. This mechanism has been shown to operate at low pH (*ca.* 3.0) in numerous studies (Compton & Daly 1984; King & Liu 1933; Nierode & Williams 1971; Berner & Morse 1974; Sjöberg & Rickard 1984; Lund *et al.* 1975; Barton & Vatatham 1976), including in the flow cell used in this work, provided the flow rates are sufficiently low (Compton & Unwin 1990).

The time-dependent convective diffusion equation is

$$\frac{\partial c}{\partial t} = D\nabla^2 c - \left(V_x \frac{\partial c}{\partial x} + V_y \frac{\partial c}{\partial y} + V_z \frac{\partial c}{\partial z} \right), \tag{11}$$

where c is the H^+ concentration and V_x, V_y, V_z are the cartesian components of the solution flow velocity.

Provided a sufficient lead in length is present upstream of the crystal surface (Compton & Unwin 1986*b*),

$$V_x = V_0[1-((y-h)^2/y)], \quad V_y = V_z = 0, \tag{12}$$

where $h = \frac{1}{2}b$.

That is the solution adopts a parabolic velocity profile with V_0 the axial velocity in the centre of the channel. Then for steady-state conditions we have,

$$D\,\partial^2 c/\partial y^2 = V_x\,\partial c/\partial x, \tag{13}$$

where we have ignored diffusion in directions other than normal to the surface of the crystal. This approximation has been thoroughly explored and has been shown to be entirely satisfactory for crystals of the size used in the work described here (Compton & Unwin 1986*b*). Providing convection within the flow cell is efficient compared with diffusion then concentration changes will be confined to being close to the wall of the channel that contains the crystal, and following Léveqûe (1928) and Levich (1962) we may write

$$V_x = V_0((2y/h)-(y^2/h^2)) \approx 2V_0 y/h. \tag{14}$$

We can replace the parabolic velocity profile by a linear one near the channel wall. Thus equation (13) becomes

$$D\frac{\partial^2 c}{\partial y^2} = (2V_0 y/h)\frac{\partial c}{\partial x}. \tag{15}$$

We define a parameter χ such that $\chi = x/x_c$, where x is the distance downstream of the upstream edge of the crystal and x_c is the crystal length, then equation (15) becomes

$$D\frac{\partial^2 c}{\partial y^2} = \frac{2V_0 y}{hx_c}\frac{\partial c}{\partial \chi}. \tag{16}$$

Further simplification results from introducing the parameter U, such that $U = (C-C_\infty)/C_\infty$, where C_∞ is the bulk H^+ concentration. Thus (16) becomes

$$D\frac{\partial^2 c}{\partial y^2} = \frac{2V_0 C_\infty y}{hx_c}\frac{\partial U}{\partial \chi}. \tag{17}$$

Solution of equation (17) is facilitated by means of the substitution

$$\xi = (2V_0 C_\infty/Dhx_c)^{\frac{1}{3}} y,$$

from which it may be shown that equation (17) becomes,

$$\partial^2 U/\partial \xi^2 = \xi\,\partial U/\partial \chi. \tag{18}$$

Solution of equation (18) *in the zone of the crystal.* In the zone of the crystal the boundary conditions are:

$$y \to \infty,\ U = 0; \quad x = 0,\ U = 0; \quad y = 0, \quad U = -1.$$

Under the Laplace transform, equation (18) becomes

$$d^2\bar{U}/d\xi^2 = s\xi\bar{U}, \tag{19}$$

where s is the Laplace transform variable. Equations of this type have the following solution in terms of Airy functions (Carrier 1968),

$$\bar{U} = A\,\mathrm{Ai}\,(s^{\frac{1}{3}}\xi) + B\,\mathrm{Bi}\,(s^{\frac{1}{3}}\xi). \tag{20}$$

Now from the boundary conditions, as $\xi \to \infty$, $\bar{U} \to 0$, we find that as $\xi \to \infty$, $\mathrm{Ai}\,(\xi) \to 0$ and $\mathrm{Bi}\,(\xi) \to \infty$ (Abramowitz & Stegun 1966). Thus we may deduce that $B = 0$, and (20) becomes

$$\bar{U} = A\,\mathrm{Ai}\,(s^{\frac{1}{3}}\xi), \tag{21}$$

where A is a constant, which may be deduced as follows. From the boundary conditions, when $\xi = 0$ then $U = -1$, the transform of this boundary condition gives us that when $\xi = 0$, $\bar{U} = -s^{-1}$. Thus when $\xi = 0$,

$$-s^{-1} = A\,\mathrm{Ai}\,(0),$$

so that

$$A = -1/s\,\mathrm{Ai}\,(0).$$

Substituting into this equation (21) gives us

$$\bar{U} = -\mathrm{Ai}\,(s^{\frac{1}{3}}\xi)/s\,\mathrm{Ai}\,(0). \tag{22}$$

Solution of equation (18) *in the zone of the sensor.* To facilitate mathematical solution in this zone we define a parameter χ_s such that $\chi_s = \chi - 1$, and split the function U into two parts U_c and U_* such that $U = U_c - U_*$, where U_c relates to the zone over the crystal and U_* to that over the sensor. Substitution of these parameters into equation (18) shows that we must now solve the equation

$$\partial^2 U_*/\partial\xi^2 = \xi\,\partial U_*/\partial\chi_s, \tag{23}$$

because U_c is already a solution of (18) as given by (22).

The boundary conditions in the region are:

$$\chi_s = 0 \quad \text{and} \quad \xi = 0, \quad U_* = 0;$$

$$\xi \to \infty, \quad U_* = 0;$$

$$y = 0, \quad \partial U_*/\partial\xi = \partial U_c/\partial\xi.$$

Again, solutions to equation (23) will be of the form

$$\bar{U}_* = G\,\mathrm{Ai}\,(p^{\frac{1}{3}}\xi), \tag{24}$$

when p is the Laplace Transform variable now with respect to χ_s. From equation (22) we obtain

$$\left.\frac{\partial\bar{U}_*}{\partial\xi}\right|_0 = -\frac{\mathrm{Ai}'\,(0)}{s^{\frac{2}{3}}\,\mathrm{Ai}\,(0)}.$$

Inversion of the above (Abramowitz & Stegun 1966) gives

$$\left.\frac{\partial U_c}{\partial\xi}\right|_0 = -\frac{\chi_c^{-\frac{1}{3}}}{\Gamma(\frac{2}{3})}\frac{\mathrm{Ai}'\,(0)}{\mathrm{Ai}\,(0)}, \tag{25}$$

and we can then use the boundary conditions specified above to show that

$$\left.\frac{\partial U_*}{\partial \xi}\right|_0 = \beta(\chi_s+1)^{-\frac{1}{3}}, \tag{26}$$

where $$\beta = -\mathrm{Ai}'(0)/\Gamma(\tfrac{2}{3})\,\mathrm{Ai}(0).$$

Because $\bar{U}_* = G\,\mathrm{Ai}(p^{\frac{1}{3}}\xi)$, then

$$\left.\frac{\partial \bar{U}_*}{\partial \xi}\right|_0 = p^{\frac{1}{3}}G\,\mathrm{Ai}'(0), \tag{27}$$

and so from equations (26) and (27) we obtain

$$p^{\frac{1}{3}}G\,\mathrm{Ai}'(0) = \beta\mathscr{L}_{\chi_s}(\chi_s+1)^{-\frac{1}{3}},$$

and $$G = (\beta/p^{\frac{1}{3}}\mathrm{Ai}'(0))\,\mathscr{L}_{\chi_s}(\chi_s+1)^{-\frac{1}{3}}. \tag{28}$$

Substitution of (28) into equation (24) gives us

$$\bar{U}_* = (\beta/p^{\frac{1}{3}}\mathrm{Ai}'(0))\,\mathrm{Ai}(p^{\frac{1}{3}}\xi)\,\mathscr{L}_{\chi_s}(\chi_s+1)^{-\frac{1}{3}}. \tag{29}$$

Now $\bar{U}(\xi=0) = \bar{U}_c(\xi=0) - \bar{U}_*(\xi=0)$, and so by substitution of equations (22) and (29) we obtain:

$$\bar{U}(\xi=0) = \frac{1}{p} - \frac{\beta\,\mathrm{Ai}(0)}{p^{\frac{1}{3}}\mathrm{Ai}'(0)}\,\mathscr{L}_{\chi_s}(\chi_s+1)^{-\frac{1}{3}}. \tag{30}$$

To complete the solution we now need to inverse Laplace Transform equation (30), which is done as follows. Let

$$p^{-\frac{1}{3}} = F_1(p) = \mathscr{L}f_1(\chi_s), \tag{31}$$

and $$\mathscr{L}(\xi_s+1)^{-\frac{1}{3}} = F_2(p) = \mathscr{L}f_2(x). \tag{32}$$

We know (Abramowitz & Stegun 1966) that

$$\mathscr{L}^{-1}p^{-\frac{1}{3}} = \chi_s^{-\frac{2}{3}}/\Gamma(\tfrac{1}{3}). \tag{33}$$

Also, the convolution theorem (Carrier 1968) tells us that

$$\mathscr{L}^{-1}F_1(p)\,F_2(p) = \int_0^{\chi_s} f_1(\chi_s - t)f_2(t)\,\mathrm{d}t, \tag{34}$$

and thus from equations (31), (32), (33) and (34) we obtain

$$\mathscr{L}^{-1}\frac{\mathscr{L}(\chi_s+1)^{-\frac{1}{3}}}{p^{\frac{1}{3}}} = \int_0^{\chi_s}\frac{1}{(\chi_s+1-t)^{\frac{1}{3}}}\frac{t^{-\frac{2}{3}}}{\Gamma(\frac{1}{3})}\,\mathrm{d}t. \tag{35}$$

Substituting equation (35) into equation (30) gives

$$U = -1 + \frac{1}{\Gamma(\frac{1}{3})\,\Gamma(\frac{2}{3})}\int_0^{\chi_s}\frac{1}{(\chi_s+1-t)^{\frac{1}{3}}t^{\frac{2}{3}}}\,\mathrm{d}t. \tag{36}$$

Integration of equation (36) by parts gives

$$U = -1 + \frac{1}{\Gamma(\frac{1}{3})\,\Gamma(\frac{2}{3})}\left[3\chi_s^{\frac{1}{3}} - \int_0^{\chi_s}\frac{t^{\frac{1}{3}}}{(\chi_s+1-t)^{\frac{4}{3}}}\,\mathrm{d}t\right]. \tag{37}$$

Now $$U = (C - C_\infty)/C_\infty,$$

so that (37) becomes

$$C = \frac{C_\infty}{\Gamma(\frac{1}{3})\,\Gamma(\frac{2}{3})}\left[3\chi_s^{\frac{1}{3}} - \int_0^{\chi_s} \frac{t^{\frac{1}{3}}}{(\chi_s+1-t)^{\frac{4}{3}}}\,\mathrm{d}t\right]. \tag{38}$$

The integral in equation (38) was evaluated numerically by replacing the integration by a summation, i.e.

$$\int_0^{\chi_s} \frac{t^{\frac{1}{3}}}{(\chi_s+1-t)^{\frac{4}{3}}}\,\mathrm{d}t = \sum_0^{\chi_s} \frac{t^{\frac{1}{3}}}{(\chi_s+1-t)^{\frac{4}{3}}}\Delta t,$$

and a satisfactory convergence was obtained with $\Delta t \approx t/5000$.

In conclusion to this section we note that we have achieved an analytical solution giving us the surface H^+ concentration downstream of the crystal. We note that the analytical theory predicts no flow rate dependence of the concentration of H^+ over the sensor surface.

(ii) *Numerical solution*

A detailed description of the BIFD method and its applicability to problems in the channel environment has been given elsewhere (Anderson & Moldoveanu 1984; Compton *et al.* 1988). In essence the method proceeds as follows. The xy plane above the crystal is covered in a two-dimensional finite difference grid. The number of grid points in the x direction is K and their separation is Δx. The number of grid points in the y direction is J, their separation being Δy. In the BIFD method we make the following approximations:

$$\partial c/\partial x = (C_{j,k+1} - C_{j,k})/\Delta x,$$

and

$$\partial^2 c/\partial y^2 = (C_{j-1,k+1} - 2C_{j,k+1} + C_{j+1,k+1})/\Delta y^2,$$

where $C_{j,k}$ is the H^+ concentration at the point whose coordinates are j, k, where j varies from 0 to J and k varies from 0 to K. The approximations mentioned above effectively linearize the concentration gradient between two grid points. We may now substitute these expressions into the convective diffusion equation for H^+, under steady-state conditions, which may be written as (Compton & Unwin 1990):

$$D\frac{\partial^2 c}{\partial y^2} - \left(\frac{6V_f}{bd}\right)\left(\frac{y}{b}\right)\left(1-\frac{y}{b}\right)\frac{\partial c}{\partial x} = 0,$$

where V_f is volume flow rate, b is the channel depth and d is the channel width. This gives us the following expression

$$\frac{D}{(\Delta y)^2}(g_{j-1,k+1} - 2g_{j,k+1} + g_{j+1,k+1}) - \frac{D}{\lambda_j(\Delta y)^2}(g_{j,k+1} - g_{j,k}) = 0, \tag{39}$$

where

$$g_{j,k} = C_{j,k}/C_\infty$$

and

$$\lambda_j = D\Delta x b^3 d/6V_f j(\Delta y)^3\,(b - j\Delta y).$$

Equation (39) simplifies to the form

$$g_{j,k} = -\lambda_j g_{j-1,k+1} + (2\lambda_j + 1)\,g_{j,k+1} - \lambda_j g_{j+1,k+1}. \tag{40}$$

The boundary conditions relevant to this problem are

(i) when $x = 0$ then $C = C_\infty$, i.e. $g_{j,0} = 1$,

(ii) when $y = 0$ then $C = 0$, i.e. $g_{0,k} = 0$,

(iii) when $y = b$ then $\partial c/\partial y = 0$, i.e. $g_{J,k} = g_{J-1,k}$.

Substituting these boundary conditions into equation (40) we get,

$$g_{1,k} = (2\lambda_1 + 1)\, g_{1,k+1} - \lambda_1 g_{2,k+1},$$

$$g_{J-1,k} = -\lambda_{J-1} g_{J-2,k+1} + (\lambda_{J-1} + 1)\, g_{J-1,k+1},$$

$$g_{j,k} = -\lambda_j g_{j-1,k+1} + (2\lambda_j + 1)\, g_{j,k+1} - \lambda_j g_{j+1,k+1} \quad \text{for} \quad j = 2 \to J-2.$$

These $J-1$ simultaneous equations may be expressed by the following matrix equation (Anderson & Moldoveanu 1984)

$$\begin{bmatrix} d_1 \\ d_2 \\ \vdots \\ d_j \\ \vdots \\ d_{J-2} \\ d_{J-1} \end{bmatrix} = \begin{bmatrix} b_1 & c_1 & & & & & 0 \\ a_2 & b_2 & c_2 & & & & \\ & \ddots & \ddots & \ddots & & & \\ & & a_j & b_j & c_j & & \\ & & & \ddots & \ddots & \ddots & \\ & & & & a_{J-1} & b_{J-2} & c_{J-2} \\ 0 & & & & & a_{J-1} & b_{J-1} \end{bmatrix} \begin{bmatrix} \mathsf{U}_1 \\ \mathsf{U}_2 \\ \vdots \\ \mathsf{U}_j \\ \vdots \\ \mathsf{U}_{J-2} \\ \mathsf{U}_{J-1} \end{bmatrix}, \tag{41}$$

where

$$d_j = g_{j,k} \quad \text{for} \quad j = 1 \to J-1,$$

$$\mathsf{U}_j = g_{j,k+1} \quad \text{for} \quad j = 1 \to J-1,$$

$$a_j = -\lambda_j \quad \text{for} \quad j = 2 \to J-1,$$

$$b_j = 2\lambda_j + 1 \quad \text{for} \quad j = 2 \to J-2,$$

$$b_{J-1} = \lambda_{J-1} + 1,$$

$$c_j = -\lambda_j \quad \text{for} \quad j = 1 \to J-2.$$

The matrix equation (41) is solved by the Thomas algorithm (Lapidus & Pinder 1968) when, if we represent equation (41) by

$$\boldsymbol{d} = T\mathsf{U},$$

the tridiagonal matrix T is factorized into two giving

$$T = T_L\, T_{\mathsf{U}},$$

or explicitly

$$T = \begin{bmatrix} \alpha_1 & & & & 0 \\ a_2 & \alpha_2 & & & \\ \ddots & \ddots & & & \\ & a_j & \alpha_j & & \\ & & \ddots & \ddots & \\ & & & a_{J-2} & \alpha_{J-2} \\ 0 & & & a_{J-1} & \alpha_{J-1} \end{bmatrix} \begin{bmatrix} 1 & \beta_1 & & & 0 \\ & 1 & \beta_2 & & \\ & & \ddots & \ddots & \\ & & & 1 & \beta_j \\ & & & \ddots & \ddots \\ & & & & 1 \quad \beta_{J-2} \\ 0 & & & & 1 \quad 1 \end{bmatrix}$$

Multiplying out we get

$$\alpha_1 = b_1,$$

$$\alpha_j = b_j - a_j \beta_{j-1} \quad \text{for} \quad j = 2 \to J-1,$$

and

$$\beta_j = c_j/\alpha_j \quad \text{for} \quad j = 1 \to J-1.$$

We now wish to find a vector $\boldsymbol{f}$ such that

$$T_L \boldsymbol{f} = \boldsymbol{d},$$

from which we get

$$f_1 = d_1/\alpha_1,$$

and

$$f_j = (d_j - (a_j f_{j-1})/\alpha_j \quad \text{for} \quad j = 2 \to J-1.$$

We now find the vector $\mathbf{U}$ from the relation

$$\boldsymbol{f} = T_{\mathrm{U}} \mathbf{U},$$

and therefore

$$\mathrm{U}_{J-1} = f_{J-1}$$

and

$$\mathrm{U}_j = f_j - (\beta_j \mathrm{U}_{j+1}).$$

In this way we calculate the vector $\mathbf{U}$ from the vector $\boldsymbol{d}$, i.e. from each vector of concentrations we may calculate the next vector downstream. Because we know the vector at the upstream edge of the crystal, we may calculate the concentrations for the entire region above the crystal.

To calculate the concentrations in the region downstream of the crystal we use essentially the same technique as described above. The exceptions being first, that the upstream boundary condition is now given by the vector relating to the downstream edge of the crystal and second, that the surface boundary condition is now a 'no flux' boundary condition, i.e.

$$g_{0,k} = g_{1,k}.$$

The equations for the g values are now given by

$$g_{1,k} = g_{1,k+1}(1+\lambda_1) - \lambda_1 g_{2,k+1},$$

$$g_{j,k} = -\lambda_j g_{j-1,k+1} + (2\lambda_j + 1)\, g_{j,k+1} - \lambda_j g_{j+1,k+1},$$

$$g_{J-1,k} = -\lambda_{J-1} g_{J-1,k+1} + (\lambda_{J-1} + 1)\, g_{J-1,k+1}.$$

The values for the elements of the tridiagonal matrix T are the same as before with the exception that now

$$b_1 = \lambda_1 + 1.$$

The equations are then solved by the same matrix formulation as shown before, enabling us to calculate H^+ concentrations at all points downstream of the crystal.

(iii) *Comparison of analytical and numerical solutions*

The surface concentration profiles for H^+ downstream of the crystal obtained by the two methods discussed above are shown in figure 3 for distances x downstream of a crystal length x_c. As can be seen, the analytical solution forms a limit to which the numerical solution approaches as the flow rate is increased. This is as we would expect, because implicit in the analytical solution is the assumption that the diffusion layer is thin compared with the channel depth. This obviously holds for fast flow rates but breaks down as they are reduced. The

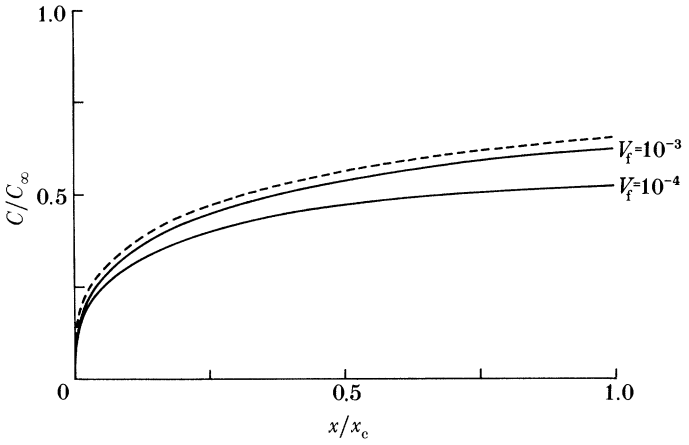

FIGURE 3. H^+ concentration profiles on the floor of the channel downstream of the crystal as predicted by: ---, analytical theory and ——, BIFD method.

numerical solution retains the full parabolic velocity profile and so should be able to predict behaviour at low flow rates much more accurately. We can also see how placing a small pH electrode close to the crystal enables us to obtain a large difference between measured concentrations on the surface and in bulk solution.

To convert these concentration profiles into predicted readings on the pH electrode the logarithms of the concentrations of H^+ on the surface of the electrode were simply averaged out. In practice it was impossible to construct the cover plates such that there was no gap between crystal and sensor, as seen in figure 2. This gap was taken into account in the averaging procedure mentioned above and the measured geometry of the crystal–sensor used to predict the observed potentiometric sensor response. In figure 4 we see how the concentration profiles from plots such as figure 3 enable us to predict readings on the pH sensor. The good agreement between the analytical and numerical solutions to the problem in the region of low pH at flow rates where we might expect agreement validates the use of the numerical technique in the region of high pH where an analytical solution is more difficult.

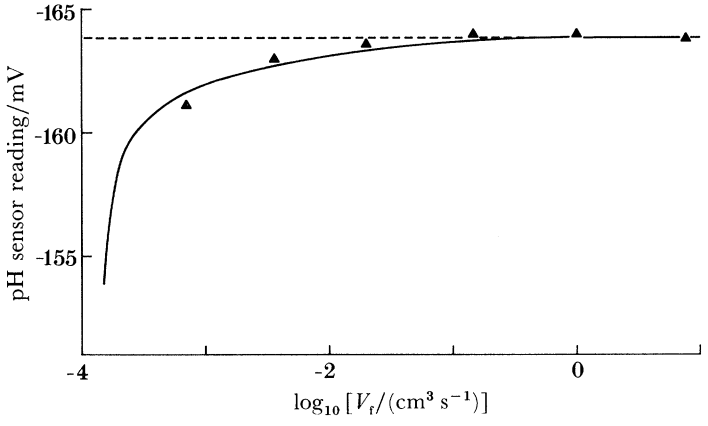

FIGURE 4. Predicted pH sensor reading variation with volume flow rate. ---, analytical theory; ——, BIFD method; △, and their comparison with experiment.

(*b*) *High* pH *region*

The overall strategy for the region of high pH is slightly more complex than for that of low pH, but has the same aim of calculating the surface H^+ concentration in the region of the pH sensor. The general strategy is as follows.

1. By using a chosen surface rate law, we first calculate Ca^{2+} concentrations in the region of the crystal.
2. Knowing the surface Ca^{2+} concentrations over the crystal, we then calculate the surface H^+, HCO_3^- and CO_3^{2-} concentrations.
3. Knowing the surface speciation, it is then possible to calculate the speciation throughout the region above the crystal taking the relevant protonation–deprotonation reactions into account.
4. From the speciation in the region above the crystal, the speciation downstream of the crystal is calculated and hence the surface speciation over the pH sensor.

(i) *Computational method*

The same basic BIFD method was used here as discussed previously with the surface rate equations being incorporated via the surface boundary condition. Thus for Ca^{2+} the surface boundary condition over the crystal becomes

$$D\left.\frac{\partial c}{\partial y}\right|_0 = F, \tag{42}$$

where F is the surface rate function and D is the Ca^{2+} diffusion coefficient. As an example of how the computation proceeds we consider the simple function proposed by Dorange & Guetchidjan (1978), i.e.

$$\text{rate} = K_{\mathrm{DG}}(1-([\mathrm{Ca}^{2+}]_{\mathrm{s}}/K_{\mathrm{sp}}^{\frac{1}{2}})),$$

where the relation to equation (1) is obvious. Equation (42) now becomes

$$\left.\frac{\partial c}{\partial y}\right|_0 = \frac{K}{D}\left(1-\frac{g_{0,k}}{K_{\mathrm{sp}}^{\frac{1}{2}}}\right).$$

Therefore

$$g_{0,k}-g_{1,k} = \frac{\Delta y K}{D}\left(1-\frac{g_{0,k}}{K_{\mathrm{sp}}^{\frac{1}{2}}}\right),$$

and

$$g_{0,k} = \left(\frac{k\Delta y}{D}+g_{1,k}\right)\left(1+\frac{K\Delta y}{DK_{\mathrm{sp}}^{\frac{1}{2}}}\right)^{-1}. \tag{43}$$

Again, the general equation for the concentration at a point j,k is given by

$$g_{j,k} = -\lambda_j g_{j-1,k+1}+(2\lambda_j+1)\,g_{j,k+1}-\lambda_j g_{j+1,k+1}. \tag{44}$$

Thus when $j=1$

$$g_{1,k} = -\lambda_1 g_{0,k+1}+(2\lambda_1+1)\,g_{1,k+1}-\lambda_1 g_{2,k+1},$$

which upon substitution of equation (43) for $g_{0,k}$ gives us

$$g_{1,k} = -(\lambda_1 K\Delta y/D)\,(1+(K\Delta y/DK_{\mathrm{sp}}^{\frac{1}{2}}))^{-1} + g_{1,k+1}[-\lambda_1(1+(K\Delta y/DK_{\mathrm{sp}}^{\frac{1}{2}}))^{-1}+2\lambda_1+1]-\lambda_1 g_{2,k+1}. \tag{45}$$

For $j = J-1$, including the 'no flux' boundary condition at the far wall of the channel gives

$$g_{J-1,k} = -\lambda_{J-1} g_{J-2,k+1} + (\lambda_{J-1}+1)\, g_{J-1,k+1}. \tag{46}$$

We solve the $J-1$ simultaneous equations given by equations (44), (45) and (46) by the same matrix formulation as shown before, giving the following matrix elements:

$$a_j = -\lambda_j \qquad \text{for} \quad j = 2 \to J-1,$$

$$b_j = (2\lambda_j + 1) \qquad \text{for} \quad j = 2 \to J-2,$$

$$c_j = -\lambda_j \qquad \text{for} \quad j = 1 \to J-2,$$

$$d_j = g_{j,k} \qquad \text{for} \quad j = 2 \to J-1,$$

$$\mathsf{U}_j = d_{j,k+1} \qquad \text{for} \quad j = 1 \to J-1,$$

$$b_1 = -\lambda_1 \left(1 + \frac{K\Delta y}{DK_{\mathrm{sp}}^{\frac{1}{2}}}\right)^{-1} + 2\lambda_1 + 1, \quad b_{J-1} = \lambda_{J-1} + 1,$$

$$d_1 = g_{1,k} + \lambda_1 \frac{K\Delta y}{D}\left(1 - \frac{K\Delta y}{DK_{\mathrm{sp}}^{\frac{1}{2}}}\right)^{-1}.$$

This matrix equation is solved again by the Thomas algorithm method, allowing us to calculate Ca^{2+} concentrations vector by vector down the crystal. The surface Ca^{2+} concentration may be calculated from the value of $g_{1,k}$ in each vector via equation (43).

The other rate equations discussed in the introduction were incorporated into the model in the same general way, with one important difference. This difference stems from the fact that the rate laws depend upon the surface concentrations of species other than Ca^{2+}. This dictates that iterative methods are used to obtain surface Ca^{2+} concentrations and the protocol is as follows. First, we take the surface Ca^{2+} concentrations predicted by the simple Dorange–Guetchidjan model and, by a method described later, calculate surface H^+, HCO_3^- and CO_3^{2-} concentrations from this. We then use these values in our new model to get an improved estimate of surface Ca^{2+} concentrations, calculate the speciations from this and repeat the process until convergence of the results is obtained. The different rate equations may very easily be incorporated into the existing framework for the numerical solution by simply slightly altering a few of the parameters. The parameters are as given for the Dorange–Guetchidjan model with the exceptions given in table 1.

We now describe how the surface Ca^{2+} concentrations generated by these calculations allow us to obtain the surface speciation for H^+, HCO_3^- and CO_3^{2-}. We assume that the reactions occurring at the surface are:

$$H_2O + CaCO_3 \to Ca^{2+} + HCO_3^- + OH^-$$

or

$$CaCO_3 \to Ca^{2+} + CO_3^{2-},$$

$$CO_3^{2-} + H_2O \rightleftharpoons HCO_3^- + OH^-,$$

and

$$H_2O \rightleftharpoons H^+ + OH^-.$$

Now, by charge conservation

$$2[Ca^{2+}] + [H^+] = 2[CO_3^{2-}] + [HCO_3^-] + [OH^-], \tag{46}$$

Table 1. Matrix elements for the backward implicit computation for different reactions

	rate $= K(1-[\mathrm{Ca^{2+}}]_s/K_{sp}^{\frac{1}{2}}))$
b_1	$-\lambda_1(1+(K\Delta y/D))^{-1}+2\lambda_1+1$
d_1	$g_{1,k}+(\lambda_1 K\Delta y/D)\,(1+(K\Delta y/DK_{sp}^{\frac{1}{2}}))^{-1}$
g_0	$((K\Delta y/D)+g_{1,k})\,(1+(K\Delta y/DK_{sp}^{\frac{1}{2}}))^{-1}$
	rate $= K(K_{sp}^{\frac{1}{2}}-[\mathrm{Ca^{2+}}]_s^{\frac{1}{2}}[\mathrm{CO_3^{2-}}]_s^{\frac{1}{2}})$
b_1	$-\lambda_1\left(1+\dfrac{K\Delta y[\mathrm{CO_3^{2-}}]_{0,k+1}^{\frac{1}{2}}}{D([\mathrm{CO_3^{2-}}]_{0,k+1}+[\mathrm{HCO_3^{-}}]_{0,k+1}^{\frac{1}{2}})}\right)^{-1}+2\lambda_1+1$
d_1	$g_{1,k}+\dfrac{\lambda_1 KK_{sp}^{\frac{1}{2}}\Delta y}{D}\left(1+\dfrac{K\Delta y[\mathrm{CO_3^{2-}}]_{0,k+1}^{\frac{1}{2}}}{D([\mathrm{CO_3^{2-}}]_{0,k+1}+[\mathrm{HCO_3^{-}}]_{0,k+1}^{\frac{1}{2}})}\right)^{-1}$
g_0	$\left(\dfrac{KK_{sp}^{\frac{1}{2}}\Delta y}{D}+g_{1,k}\right)\left(1+\dfrac{K\Delta y[\mathrm{CO_3^{2-}}]_{0,k+1}^{\frac{1}{2}}}{D([\mathrm{CO_3^{2-}}]_{0,k+1}+[\mathrm{HCO_3^{-}}]_{0,k+1}^{\frac{1}{2}})}\right)^{-1}$
	rate $= k-k[\mathrm{Ca^{2+}}]_s[\mathrm{HCO_3^{-}}]_s$
b_1	$-\lambda_1(1+(k'[\mathrm{HCO_3^{-}}]_{0,k+1}\Delta y/D))^{-1}+2\lambda_1+1$
d_1	$g_{1,k}+(\lambda_1 k\Delta y/D)\,(1+(k'[\mathrm{HCO_3^{-}}]_{0,k+1}\Delta y/D))^{-1}$
g_0	$((k\Delta y/D)+g_{1,k})\,(1+(k'[\mathrm{HCO_3^{-}}]_{0,k+1}/D))^{-1}$

and because the calcium carbonate dissolved stoichiometrically

$$[\mathrm{Ca^{2+}}]=[\mathrm{CO_3^{2-}}]+[\mathrm{HCO_3^{-}}]. \tag{47}$$

We know also that

$$K_A=[\mathrm{CO_3^{2-}}]\,[\mathrm{H^+}]/[\mathrm{HCO_3^{-}}], \tag{48}$$

and

$$K_w=[\mathrm{H^+}]\,[\mathrm{OH^-}]. \tag{49}$$

From equations (47) and (48) we obtain

$$K_A=\frac{[\mathrm{CO_3^{2-}}]\,[\mathrm{H^+}]}{[\mathrm{Ca^{2+}}]-[\mathrm{CO_3^{2-}}]}, \tag{50}$$

from equations (46) and (47)

$$[\mathrm{CO_3^{2-}}]=[\mathrm{Ca^{2+}}]+[\mathrm{H^+}]-[\mathrm{OH^-}], \tag{51}$$

and thus from equations (50) and (51) we obtain

$$K_A=\frac{([\mathrm{Ca^{2+}}]+[\mathrm{H^+}]-(K_w/[\mathrm{H^+}]))\,[\mathrm{H^+}]}{(K_w/[\mathrm{H^+}])-[\mathrm{H^+}]},$$

or

$$[\mathrm{H^+}]^3+[\mathrm{H^+}]^2\,([\mathrm{Ca^{2+}}]+K_A)-[\mathrm{H^+}]\,K_w-K_w k_2=0. \tag{52}$$

This cubic equation is solved by a Newton–Raphson iterative method to give the surface H^+ concentration. Knowing both the surface H^+ and Ca^{2+} concentrations we may then calculate surface CO_3^{2-} concentrations from equation (51) and surface HCO_3^- concentrations from equation (47).

Thus our calculations so far have given us the Ca^{2+} concentration profile throughout the solution above the crystal and the surface speciation. We may now calculate the concentration profiles of the other species using the same numerical techniques, with the surface concentrations calculated above acting as the surface boundary conditions. To illustrate this

consider HCO_3^-, for which we need to take account not only of its diffusion and convection away from the crystal but also the effect of deprotonation on its concentration profile, i.e.

$$HCO_3^- \underset{k_2}{\overset{k_1}{\rightleftharpoons}} CO_3^{2-} + H^+.$$

The convective diffusion equation is modified by these kinetics to give,

$$D\frac{\partial c^2}{\partial y^2} - \left(\frac{6V_f}{bd}\right)\left(\frac{y}{b}\right)\left(1-\frac{y}{b}\right)\frac{\partial c}{\partial x} + k_2[CO_3^{2-}]\,[H^+] - k_1[H^+] = 0.$$

This is then treated in the same way as shown previously for the BIFD method giving the following elements in the tridiagonal matrix:

$$a_j = -\lambda_j \qquad \text{for} \quad j = 2 \to J-1,$$

$$b_j = 2\lambda_j + 1 \qquad \text{for} \quad j = 1 \to J-2,$$

$$b_{J-1} = (\lambda_{J-1} + 1)$$

$$c_j = -\lambda_j \qquad \text{for} \quad j = 1 \to J-2,$$

$$d_j = g_{j,k}(1 - (k_1\lambda_j(\Delta y)^2/D)) + (\lambda_j(\Delta y)^2 k_2[CO_3^{2-}]_{j,k}\,[H^+]_{j,k}/D),$$

$$d_1 = g_{j,k}(1 - (k_1\lambda_j(\Delta y)^2/D)) + (\lambda_j(\Delta y)^2 k_2[CO_3^{2-}]_{j,k}\,[H^+]_{j,k}/D) + \lambda_1[HCO_3^-]_{0,k+1}.$$

The upstream boundary condition is simply the concentration of the species in the reservoir supply and the surface boundary condition is the surface concentration calculated previously. This surface boundary condition comes into the calculation in the expression for d_1.

The concentration profiles for the other species are calculated in the same way, with the following alterations to d_j and d_1. For the H^+ calculations

$$d_j = g_{j,k}(1 - (k_2\lambda_j(\Delta y)^2\,[CO_3^{2-}]_{j,k}/D)) + (\lambda_j(\Delta y)^2 k_1[HCO_3^-]_{j,k}/D),$$

and $$d_1 = g_{j,k}(1 - (k_2\lambda_j(\Delta y)^2\,[CO_3^{2-}]_{j,k}/D)) + (\lambda_j(\Delta y)^2 k_1[HCO_3^-]_{j,k}/D) + \lambda_1[H^+]_{0,k+1}.$$

For the CO_3^{2-} calculations

$$d_j = g_{j,k}(1 - (k_2\lambda_j(\Delta y)^2\,[H^+]_{j,k}/D)) + (\lambda_j(\Delta y)^2 k_1[HCO_3^-]_{j,k}/D),$$

and $$d_j = g_{j,k}(1 - (k_2\lambda_j(\Delta y)^2\,[H^+]_{j,k}/D)) + (\lambda_j(\Delta y)^2 k_1[HCO_3^-]_{j,k}/D) + \lambda_1[CO_3^{2-}]_{0,k+1}.$$

So we now know the concentration profile of all the species in the region above the crystal, and from this may calculate their profiles in the region downstream of the crystal. Again we use the BIFD method but with the upstream boundary condition given by the concentration profiles at the downstream edge of the crystal and the surface boundary condition a simple 'no flux' condition. This procedure produces the following matrix elements for H^+.

$$a_j = -\lambda_j \qquad \text{for} \quad j = 2 \to J-1,$$

$$b_j = 2\lambda_j + 1 \qquad \text{for} \quad j = 2 \to J-2,$$

$$b_1 = \lambda_1 + 1, \quad b_{J-1} = \lambda_{J-1} - 1, \quad c_j = -\lambda_j \quad \text{for} \quad j = 1 \to J-2,$$

$$d_j = g_{j,k}(1 - (\lambda_j k_2(\Delta y)^2\,[CO_3^{2-}]_{j,k}/D)) + (\lambda_j(\Delta y)^2 k_1[HCO_3^-]_{j,k}/D).$$

PHILOSOPHICAL TRANSACTIONS OF THE ROYAL SOCIETY A MATHEMATICAL, PHYSICAL & ENGINEERING SCIENCES

For CO_3^{2-} the matrix elements are the same as for H^+ with the sole exception that,

$$d_j = g_{j,k}(1-(\lambda_j k_2 \lambda_j(\Delta y)^2[H^+]_{j,k}/D)) + (\lambda_j(\Delta y)^2 k_1[HCO_3^-]_{j,k}/D),$$

and for HCO_3^- the elements are again the same but for

$$d_j = g_{j,k}(1-(\lambda_j k_1(\Delta y)^2/D)) + (\lambda_j(\Delta y)^2 k_2[CO_3^{2-}]_{j,k}[H^+]_{j,k}/D).$$

The no flux boundary condition at the surface tells us that $g_{0,k} = g_{1,k}$ so we are able to calculate the surface speciation downstream of the crystal. From this we are able to calculate the response of the pH electrode for each surface rate equation as a function of a single kinetic parameter.

The constants used in the theoretical work were all corrected for activity effects, to correspond to the experimental ionic strength of 0.5 mol dm^{-3}. As an example of how this was done consider the second dissociation constant of carbonic acid. If we use a mixed acidity constant,

$$K_{A'} = a_{H^+}[CO_3^{2-}]/[HCO_3^-],$$

we need to correct the value obtained from reference data (Stumm & Morgan 1981), which is a value for infinite dilution, i.e.

$$K_{A^0} = a_{H^+} a_{CO_3^{2-}}/a_{HCO_3^-}$$

thus

$$k_{A'} = K_{A^0}\gamma_{HCO_3^-}/\gamma_{CO_3^{2-}}.$$

The relevant activity coefficients were then obtained from the literature (Walker *et al.* 1927) and the necessary correction to the standard data was made. The values of the constants used are shown in table 2.

Table 2. Parameters used in the backward implicit modelling

K_{sp} (calcite solubility product)	1.331×10^{-8} mol^2 dm^{-6}
K_{A2} (2nd dissociation constant of carbonic acid)	1.409×10^{-10} mol dm^{-3}
K_w (dissociation constant of water)	1.008×10^{-14} mol^2 dm^{-6}

4. Results

(*a*) *Low* pH *region*

In figure 4 we showed the predicted sensor readings as a function of flow rate for both the analytical and numerical solutions to the problem. Also shown are experimental results obtained using an aqueous solution of HCl of pH = 2.1 flowing over a crystal 0.4 cm long. We can see that there is good agreement between the analytical theory and experiment at flow rates above 10^{-2} cm^3 s^{-1}, but below this the agreement breaks down. However, the numerical solution is in good agreement over the entire flow rate range used. This validates the use of the BIFD method as a means of solution of this type of problem, and illustrates that the hydrodynamics within the cell are adequately described by the convective diffusion equations presented above.

(*b*) *High* pH *region*

The results for the three candidate surface mechanisms are presented in figures 5–7 for an experiment performed at pH = 7.49, with a crystal of length 0.66 cm, and polished with 0.25 μm diamond grit. Flow rates between 10^{-3} and 0.5 cm^3 s^{-1} were used and the cell thermostatted as (25 ± 0.2) °C. Figure 5 shows the best fits for a mechanism of the

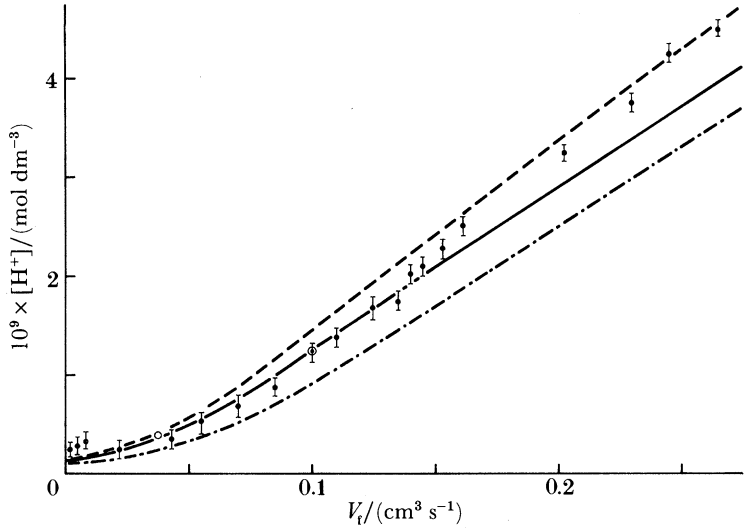

FIGURE 5. Comparison of predicted pH sensor reading for a surface rate equation of the Dorange–Guetchidjan type with experiment for bulk solution pH = 7.49. ---, $K_{DG} = 1.31 \times 10^{-3}$ mol cm s^{-1}; ——, $K_{DG} = 1.48 \times 10^{-3}$ mol cm s^{-1}; –·–·–, $K_{DG} = 1.60 \times 10^{-3}$ mol cm s^{-1}.

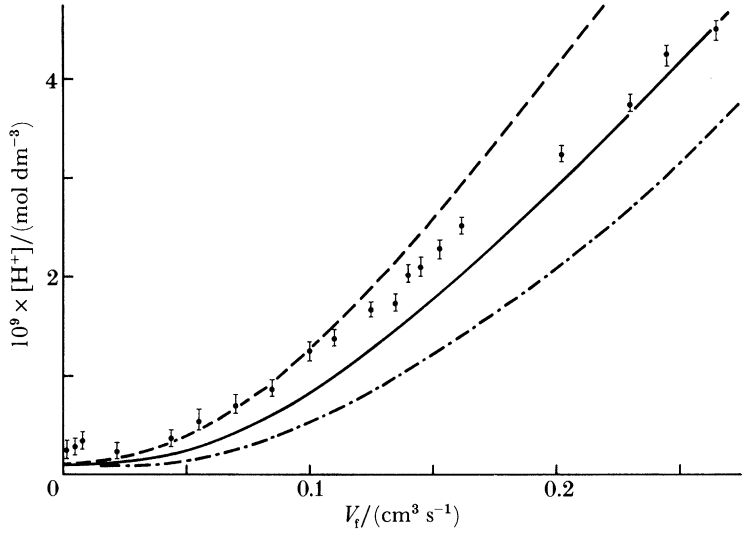

FIGURE 6. Comparison of predicted pH sensor reading for a surface rate equation of the Sjöberg type with experiment for bulk solution pH = 7.49. ---, $K_s = 1.85 \times 10^{-3}$ mol cm s^{-1}; ——, $K_s = 2.4 \times 10^{-3}$ mol cm s^{-1}; –·–·–, $K_s = 3.0 \times 10^{-3}$ mol cm s^{-1}.

Dorange–Guetchidjan type, i.e. equation (1), with the closest fit being obtained, by eye, for a rate constant $K^*_{DG} = 1.48 \times 10^{-3}$ mol cm s^{-1}. However, even the best fit is far from satisfactory, especially at faster flow rates. In figure 6 are the corresponding fits for a mechanism of the Sjöberg type, i.e. equation (2). Here the optimum fit is obtained with $K_s = 2.4 \times 10^{-3}$ mol cm s^{-1}, but again the fit is generally poor. In figure 7 we show the result obtained for the Plummer type mechanistic equation, i.e. equation (3). The agreement between the experimental and theoretical results, with $k = 9.5 \times 10^{-11}$ mol cm^{-2} s^{-1}, is excellent.

Experiments were repeated with a bulk solution of pH of 8.46 and the same experimental

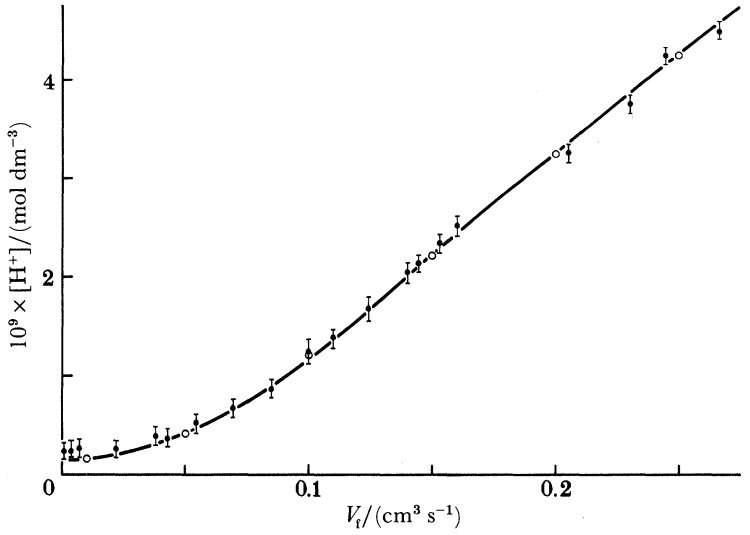

FIGURE 7. Comparison of predicted pH sensor reading, for a surface rate equation of the Plummer type, with experiment for bulk solution pH = 7.49, $k = 9.5 \times 10^{-11}$ mol cm^{-2} s^{-1}.

parameters as before, the results of which are shown in figures 8–10 along with results obtained using the three model equations with the 'best fit' rate constants obtained at pH 7.49. The correlation between the experimental and theoretical data is good, showing the pH dependence of the model data to be accurate. Thus the kinetic parameters show no pH dependence, which is in accordance with all experimental work done in this pH range (Dorange & Guetchidjan 1978; Sjöberg 1976, 1978; Plummer *et al.* 1978; Erga & Terjesen 1956; Sjöberg & Rickard 1984). Once again the best fit is obtained from the Plummer equation (3), which leads us to choose this as the rate equation that best describes the dissolution processes taking place at the calcite crystal surface, from those tested. Note, however, that our form of the Plummer equation uses surface, not the bulk concentrations that were originally proposed.

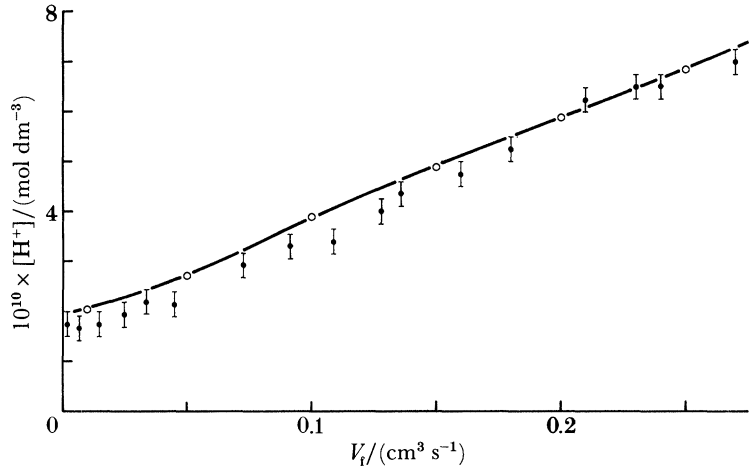

FIGURE 8. Comparison of predicted pH sensor reading, for a surface rate equation of the Dorange–Guetchidjan type, with experiment for bulk solution pH = 8.46, and $k_{DG} = 1.48 \times 10^{-3}$ mol cm s^{-1}.

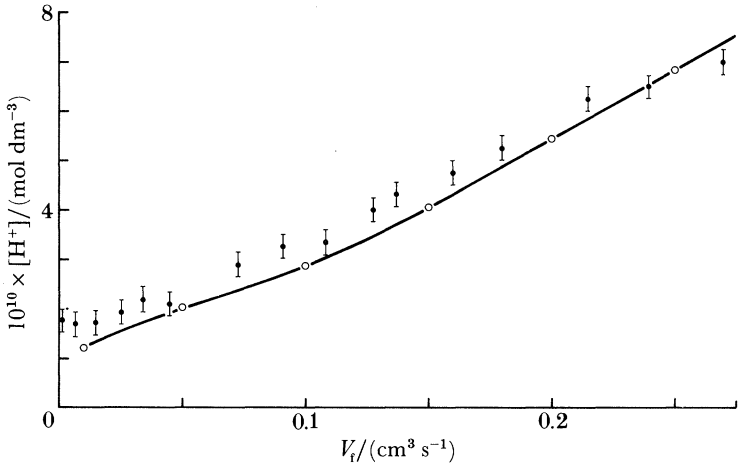

FIGURE 9. Comparison of predicted pH sensor reading, for a surface rate equation of the Sjöberg type, with experiment for bulk solution pH = 8.46, and $K_s = 2.4 \times 10^{-3}$ mol cm s^{-1}.

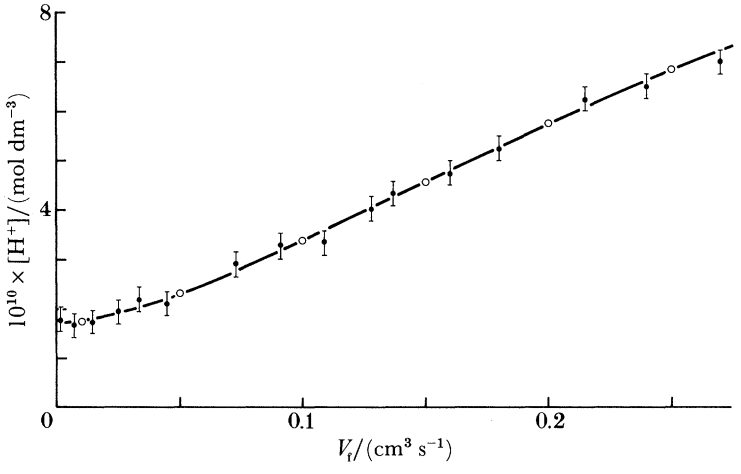

FIGURE 10. Comparison of predicted pH sensor reading, for a surface rate equation of the Plummer type, with experiment for bulk solution pH = 8.46, and $k = 9.5 \times 10^{-11}$ mol cm^{-2} s^{-1}.

We showed earlier that in equation (3) the rate constant k' is related to k by the relation $k' = k/K_{sp}$, so that the Plummer type mechanism may be written as

$$\text{rate (mol cm}^{-2}\ \text{s}^{-1}) = 9.5 \times 10^{-11} - 7.14 \times 10^{-3}[Ca^{2+}]_s\,[[CO_3^{2-}]_s. \qquad (53)$$

In table 3 we show some of the results obtained from the modelling work using the above equation and the experimental conditions described above for the runs done at pH 7.49.

From this we see how, as we reduce the flow rate, we allow a greater build up of reaction products on the surface. This in turn increases the second term in our rate equation (53) and so reduces the flux from the surface. We would also expect that as we go further down the crystal we would get a decrease in the reaction rate caused by the build up of reaction products. In figure 11 we show the flux from the surface for these different flow rates as a function of distance x down a crystal of length x_c where $x_c = 0.66$ cm. The computed fluxes show the expected decrease.

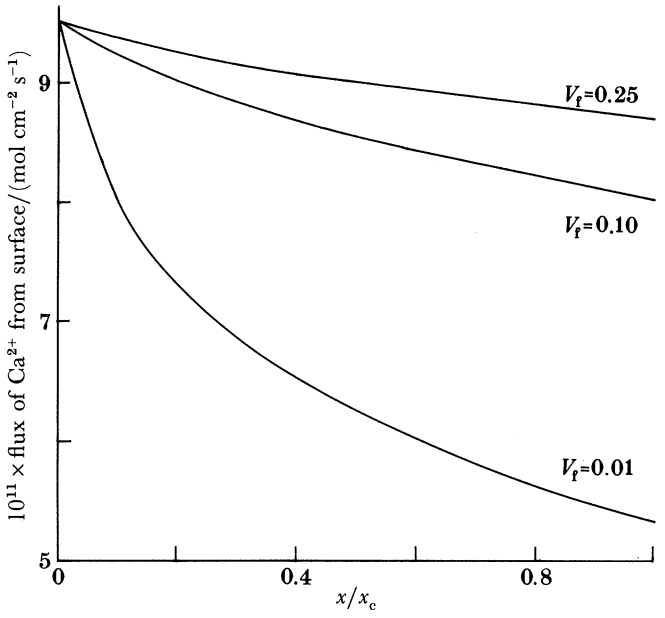

FIGURE 11. Flux of Ca^{2+} from the surface predicted by equation (5) with $k = 9.5 \times 10^{-11}$, as a function of distance x down the crystal length x_c and flow rate.

TABLE 3. RESULTS OBTAINED FROM EQUATION (53)

V_f (cm^3 s^{-1})	10^{11} × flux (mol cm^{-2} s^{-1})	10^{10} × [H^+] measured (mol dm^{-3})	10^7 × bulk[Ca^{2+}] (mol dm^{-3})
0.25	9.03	42.5	1.36
0.20	8.95	32.6	1.68
0.15	8.83	22.2	2.21
0.10	8.61	12.1	3.24
0.05	8.13	41.9	6.11
0.01	6.51	17.3	24.4

In figure 12 we show the concentration profiles for all the species concerned in the region above and downstream of the crystal, under the conditions described for the pH 7.49 experiments at a flow rate of 0.01 cm^3 s^{-1}. The plots show the concentration profiles in the xy plane with the z axis representing concentration. The plots relating to the region over the crystal show the expected increase in concentration as we go down the crystal, for the reaction products. We can also see the depletion of the H^+ concentration caused by the following reaction,

$$H_2O + CO_3^{2-} \rightleftharpoons HCO_3^- + OH^-.$$

The plots in the region downstream of the crystal show the decrease in product concentration on the channel floor as we go further away from the crystal and the continued diffusion of these products into the bulk solution.

The results presented above show once again how important the precise hydrodynamics of the system are. The flux variations with the flow rate shows that to make predictions about dissolution rates under conditions different from our particular experiments we require a detailed knowledge of the hydrodynamics involved in the systems of interest.

The maximum dissolution rate that this model would predict is one of 9.5×10^{-11} mol cm^{-2} s^{-1}

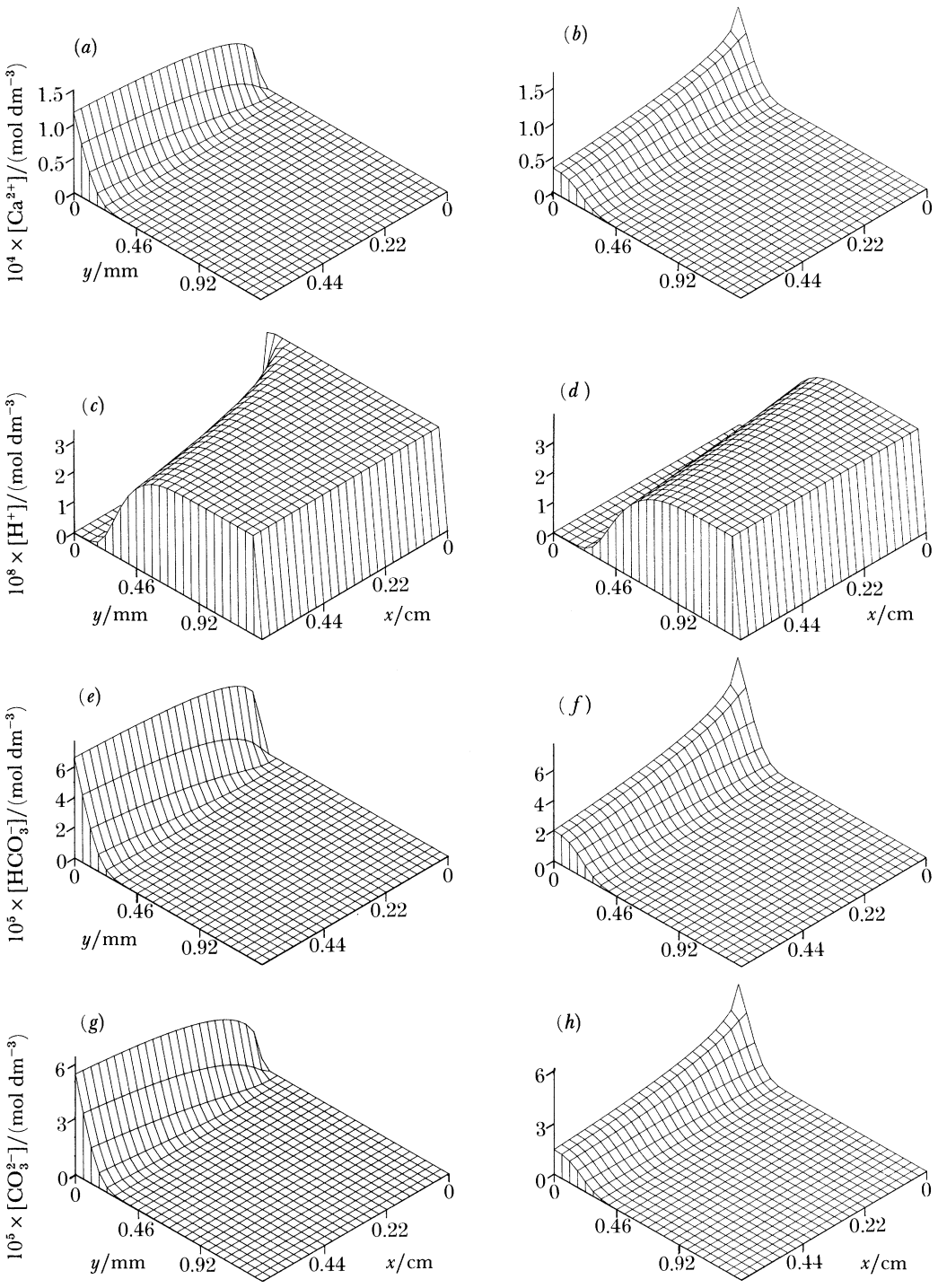

FIGURE 12. Three-dimensional plots in which the z direction represents concentration in the xy plane both over and downstream of the crystal, for a crystal length of 0.66 cm, a flow rate of 1×10^{-2} cm^3 s^{-1} and a pH = 7.49. This data represents the results from the modelling work using the Plummer type equation. (*a*) Ca^{2+} over the crystal, (*b*) Ca^{2+} downstream of the crystal, (*c*) H^+ over the crystal, (*d*) H^+ downstream of the crystal, (*e*) HCO_3^- over the crystal, (*f*) HCO_3^- downstream of the crystal, (*g*) CO_3^{2-} over the crystal, (*h*) CO_3^{2-} downstream of the crystal.

PHILOSOPHICAL TRANSACTIONS OF THE ROYAL SOCIETY A MATHEMATICAL, PHYSICAL & ENGINEERING SCIENCES

which is approached for small crystals and high flow rates. This is to be compared with Plummer's experimental results (for rate equations using bulk concentrations) in which initial rate of dissolution of 1.2×10^{-10} mol cm^{-2} s^{-1}. Previous work (Compton *et al.* 1986*a*) has shown the importance of surface morphology effects on dissolution. Thus it is important to consider the different surface preparations used in both cases. The powders used in Plummer's work were washed in dilute HCl, which will cause a degree of pitting. In our experiments the crystal surface was polished with a succession of grit sizes down to 0.25 μm. Thus the surface of our crystal is liable to be smoother than those of Plummer's powders and so we might expect our maximum flux to be smaller than that obtained by Plummer. In the work published by Sjöberg using rotating calcite discs (Sjöberg & Rickard 1983) a rate constant of 7×10^{-10} mol cm^{-2} s^{-1} was observed. In that work the crystal preparation involved polishing to 30 μm then etching in 10^{-2} M HCl. This procedure is liable to produce a much rougher surface than our preparation and may account for the larger rate constant measured.

5. Conclusion

We have described a new technique that may be applied to the study of the dissolution of calcite under high pH conditions and have developed a general computational technique that allows us to probe the surface rate law and discriminate between candidate dissolution mechanisms. This work has led us to choose the following rate equation as the one that best describes the rate of dissolution in terms of surface speciation

$$\text{rate (mol cm}^{-2}\text{ s}^{-1}) = k - k'[\text{Ca}^{2+}]_s\,[\text{CO}_3^{2-}]_s,$$

when $k' = k/K_{sp}$, and k is dependent upon surface morpology.

We emphasize this equation has a fundamental difference from other equations that attempt to describe dissolution, in that it deals with concentrations at the surface of the crystal rather than bulk solution concentrations. It should not be necessary for us to point out that because the surface is the region where dissolution takes place, the surface concentrations must have a more fundamental part to play in the kinetics than concentrations measured at some distance from the surface in bulk solution. We thus conclude that the equation given above is the most physically significant equation yet proposed for the dissolution of calcite.

We thank the NERC and the Freshwater Biological Association for a CASE studentship for K. L. P., Patrick Unwin and Alan House for useful discussions, Margot Long for typing the manuscript and the late David Koslow for producing the figures.

References

Abramowitz, M. & Stegun, I. A. 1966 *Handbook of mathematical functions*. New York: Dover.
Anderson, J. L. & Moldoveanu, S. 1984 *J. electroanal. Chem.* **179**, 107–119.
Barton, P. & Vatatham, T. 1976 *Environ. Sci. Technol.* **10**, 262–266.
Berner, R. A. & Morse, J. W. 1974 *Am. J. Sci.* **274**, 108–134.
Carrier, G. F. 1968 *Differential equations*. London: Blaisdell.
Compton, R. G. & Daly, P. J. 1984 *J. Colloid Interface Sci.* **101**, 159–166.
Compton, R. G., Daly, P. J. & House, W. A. 1986*a* *J. Colloid Interface Sci.* **113**, 12–20.
Compton, R. G., Pilkington, M. B. G. & Stearn, G. M. 1988 *J. Chem. Soc. Faraday Trans.* I **84**, 2155–2171.
Compton, R. G. & Unwin, P. R. 1986*b* *J. electroanal. Chem.* **205**, 1–46.
Compton, R. G. & Unwin, P. R. 1990 *Phil. Trans. R. Soc. Lond.* A **330**, 1–45. (Previous paper.)

PHILOSOPHICAL TRANSACTIONS OF THE ROYAL SOCIETY A MATHEMATICAL, PHYSICAL & ENGINEERING SCIENCES

Dorange, G. & Guetchidjan, A. 1978 *C.r. hebd. Séanc Acad. Sci., Paris*, Ser. C, 159–162.
Erga, O. & Terjesen, S. G. 1956 *Acta. chem. scand.* A **10**, 872–874.
King, C. V. & Liu, C. L. 1933 *J. Am. chem. Soc.* **55**, 1928–1940.
Lapidus, L. & Pinder, G. F. 1968 *Numerical solution of partial differential equations*, 2nd edn. New York: John Wiley.
Léveqûe, M. A. 1928 *Annls Mines Mem.* ser. 12, 13–201.
Levich, V. G. 1962 *Physiochemical hydrodynamics*. Englewood Cliffs, New Jersey: Prentice-Hall.
Lund, K., Fogler, H. S., McCune, C. C. & Ault, J. W. 1975 *Chem. Engng Soc.* **30**, 825–835.
Nierode, D. E. & Williams, B. B. 1971 *Soc. Pet. Engrs J.* **11**, 406–481.
Plummer, L. N., Wigley, T. M. & Parkhurst, D. L. 1978 *Am. J. Sci.* **208**, 179–216.
Sjöberg, E. L. 1976 *Geochim. cosmochim. Acta* **40**, 441–447.
Sjöberg, E. L. 1978 *Stockh. Contr. Geol.* **32**, 1–96.
Sjöberg, E. L. & Rickard, D. 1983 *Geochim. cosmochim. Acta* **47**, 2281–2292.
Sjöberg, E. L. & Rickard, D. 1984 *Chem. Geol.* **42**, 119–136.
Stumm, W. & Morgan, J. J. 1981 *Aquatic chemistry*, 2nd edn. New York: Wiley.
Walker, A. C., Bray, U. B. & Johnston, J. 1927 *J. Am. chem. Soc.* **49**, 1235–1261.

PHILOSOPHICAL TRANSACTIONS OF THE ROYAL SOCIETY A MATHEMATICAL, PHYSICAL & ENGINEERING SCIENCES